Backward Finite-Time Lyapunov Exponents in Inertial Flows

Tobias Günther and Holger Theisel

Fig. 1: Backward FTLE of inertial particles as computed from influence curves [28] (left) correlates with preferential particle settling (center). In previous work, particle settling has been analyzed by backward FTLE on tracer particles [66] (right), which shows resemblance but is not as accurate. Here, in the DOUBLE GYRE with $d_p = 200\,\mu m$, start time $t_0 = 0$ and integration duration $\tau = 9$.

Abstract— Inertial particles are finite-sized objects that are carried by fluid flows and in contrast to massless tracer particles they are subject to inertia effects. In unsteady flows, the dynamics of tracer particles have been extensively studied by the extraction of Lagrangian coherent structures (LCS), such as hyperbolic LCS as ridges of the Finite-Time Lyapunov Exponent (FTLE). The extension of the rich LCS framework to inertial particles is currently a hot topic in the CFD literature and is actively under research. Recently, backward FTLE on tracer particles has been shown to correlate with the preferential particle settling of small inertial particles. For larger particles, inertial trajectories may deviate strongly from (massless) tracer trajectories, and thus for a better agreement, backward FTLE should be computed on inertial trajectories directly. Inertial backward integration, however, has not been possible until the recent introduction of the influence curve concept, which – given an observation and an initial velocity – allows to recover all sources of inertial particles as tangent curves of a derived vector field. In this paper, we show that FTLE on the influence curve vector field is in agreement with preferential particle settling and more importantly it is not only valid for small (near-tracer) particles. We further generalize the influence curve concept to general equations of motion in unsteady spatio-velocity phase spaces, which enables backward integration with more general equations of motion. Applying the influence curve concept to tracer particles in the spatio-velocity domain emits streaklines in massless flows as tangent curves of the influence curve vector field. We demonstrate the correlation between inertial backward FTLE and the preferential particle settling in a number of unsteady vector fields.

Index Terms—Inertial particles, finite-time Lyapunov exponents, backward integration, preferential particle settling.

◆

---

1 INTRODUCTION

Inertial particles are small objects with a certain diameter and density, which are immersed in and transported by fluid flows, e.g., sand particles in air. The trajectories of inertial particles are not tangential to the underlying flow, but can be understood as tangent curves of a higher dimensional vector field [25, 28] and thus they have recently gained recognition as a new problem to apply ideas and methods from the vast body of flow visualization research to, including integral geometry [23], vortex extraction [25], finite-time separation [26] and vector field topology [27]. In traditional flow visualization of massless tracer particles, Lagrangian coherent structures (LCS) were established as effective means to capture the dynamics of unsteady flows. Recently, Haller [30] reviewed the work on LCS for massless particles and pointed out that the well-formed theory for massless particles is now underway to be extended to the inertial case. Recent work [47, 66] focused on hyperbolic (forward) LCS in inertial flows via finite-time Lyapunov exponents (FTLE), i.e., material surfaces that separate locally the strongest. Backward FTLE is an established indicator for reverse-time hyperbolic LCS, which reveal attractors in the flow. Alternatively, preferential particle settling can be seen as a brute force method that emits a large number of particles and finds attractors via density estimates. Sudharsan et al. [66] have shown that for small particles, backward FTLE on tracer particles correlates with inertial preferential particle settling. However, the larger a particle the more its trajectory deviates from the track of a massless tracer particle. Thus, we argue that for a stronger agreement with preferential particle settling, FTLE should be computed from *inertial backward trajectories*. However, inertial backward integration is problematic in theory and practice, due to the strong repelling behavior in the phase space [27]. Recently, Günther and Theisel introduced *influence curves* [28], which allow to recover the origin of an inertial particle for a given initial velocity (in contrast to approximations [31]).

In this paper, we generalize influence curves to general equations of motion in unsteady spatio-velocity phase spaces and apply this to compute backward FTLE of inertial particles. Using the equations of motion described in Crowe et al. [17] and the ones in Haller and Sapsis [31], we show that inertial backward FTLE based on influence curves is in agreement with preferential particle settling, see Fig. 1. We demonstrate the impact of the initial velocity and gravity, which have both been neglected in [66]. We further show that for massless flows, streakline vector fields [72] are a special case of our generalized influence curve description. Further, we demonstrate that influence curves can be used to calculate other Lagrangian measures in backward time, e.g., finite-time mass separation [26] and accumulated curvature. We test our technique on a number of analytic and real-world flows in 2D, and one example in 3D.

2 BACKGROUND AND RELATED WORK

Finite-sized objects are relevant in many application areas and as categorized by Sudharsan et al. [66], inertial particles were used to assess turbulence [5, 6, 8, 18, 52, 53, 63], gravitational settling velocity and set-

tling time [40,41,49,55,65], and the preferential particle settling after advection for a certain duration. The latter found applications in meteorology [12,59,62], sand saltation modeling [61], soiling of cars [54], plant spores and pathogens carried by atmospheric flow [13], urban pollution [68], the tracking of toxic elements [44], plankton dynamics in jellyfish feeding [46], visual obscuration in helicopter landing [37] and the capture of inertial particles in aquatic systems [19].

In the following section, we introduce into the modeling of inertial particles and review recent work on the extraction of finite-time Lyapunov exponents (FTLE). Afterwards, we touch upon visualization work regarding inertial particles, including the meaning of FTLE for inertial particles. Finally, we discuss the difficulties of inertial backward integration, which motivates our method.

2.1 Equation of Motion of Inertial Particles

Inertial particles have a finite size and thus, in contrast to massless tracer particles, they are affected by inertia and gravity. Today's most accepted form of the equations of motion goes back to the seminal work of Maxey and Riley [42]. The properties of their model and the history of its improvements were recently documented by Farazmand and Haller [20].

Depending on the application, assumptions can be made that simplify the equations considerably. The majority of the examples in this paper uses the model described in Crowe et al. [17], i.e., we assume that particles are very small and that the density of the surrounding air is far smaller than the density of the particles. The model assumes one-way coupling, i.e., particles have no influence on the underlying flow. Also, particle-particle interactions are neglected. These assumptions are common in practice [7,10,15,37,48,52,67] and lead to a simplified set of equations of motion, as described next.

2.1.1 Inertial Phase Spaces

Under the aforementioned assumptions, Günther and Theisel [25,26] described the trajectories of inertial particles as tangent curves of a high-dimensional phase space $\hat{\mathbf{p}}$, which models both the rate of change of particle position $\mathbf{x}$ and particle velocity $\mathbf{v}$. For an unsteady underlying flow $\mathbf{u}(\mathbf{x},t)$ in n-D with $n \in \{2,3\}$, the autonomous governing m-D vector field, with $m = 2n + 1$, becomes:

$$\hat{\mathbf{p}} = \frac{d}{dt}\begin{pmatrix}\mathbf{x}\\\mathbf{v}\\t\end{pmatrix} = \begin{pmatrix}\mathbf{v}\\\frac{\mathbf{u}(\mathbf{x},t)-\mathbf{v}}{r}+\mathbf{g}\\1\end{pmatrix} \text{ with } \begin{pmatrix}\mathbf{x}\\\mathbf{v}\\t\end{pmatrix}(0) = \begin{pmatrix}\mathbf{x}_0\\\mathbf{v}_0\\t_0\end{pmatrix} \quad (1)$$

where $\mathbf{g}$ is a gravity vector (if not mentioned otherwise we set $\mathbf{g} = \mathbf{0}$), and $\mathbf{x}_0$, $\mathbf{v}_0$ and t_0 are the initial particle position, velocity and time. Response time r is defined by particle diameter d_p and particle density ρ_p, as well as the viscosity μ of the surrounding air:

$$r = \frac{d_p^2 \rho_p}{18\mu} > 0 \quad (2)$$

Throughout the paper, we set as particle density ρ_p the density of dry sand, i.e., $\rho_p = 1600\,kg/m^3$. The diameter d_p was set between $200\,\mu m$ and $500\,\mu m$. The surrounding medium was assumed to be air, thus the viscosity was set to $\mu = 1.532 \cdot 10^{-5}\,kg/(m\cdot s)$. Given these parameters, r is in our experiments in the range $r \in [0.232, 1.450]$.

Another common model explicitly incorporates the density ratio R between inertial particles and the surrounding medium, which allows to include buoyancy effects [31], i.e., it allows to distinguish between aerosols ($R < 2/3$), neutrally buoyant particles ($R = 2/3$) and bubbles ($R > 2/3$). Expressed as an autonomous ODE we get:

$$\hat{\mathbf{p}} = \frac{d}{dt}\begin{pmatrix}\mathbf{x}\\\mathbf{v}\\t\end{pmatrix} = \begin{pmatrix}\mathbf{v}\\\frac{R}{St}(\mathbf{u}(\mathbf{x},t)-\mathbf{v})+\frac{3R}{2}\frac{D\mathbf{u}(\mathbf{x},t)}{Dt}+(1-\frac{3R}{2})\mathbf{g}\\1\end{pmatrix} \quad (3)$$

with St being the Stokes number ($St \to 0$ for massless particles) and

$$\frac{D\mathbf{u}(\mathbf{x},t)}{Dt} = \nabla\mathbf{u}\cdot\mathbf{u} + \mathbf{u}_t, \qquad R = \frac{2\rho_f}{\rho_f + 2\rho_p}. \quad (4)$$

Here, ρ_p and ρ_f denote the density of a particle and the fluid, respectively. Variants of this phase space have been used in [2,9,66,71], where gravity-free and/or neutrally buoyant particles were assumed.

While the majority of the examples in this paper uses Eq. (1), our generalization of the influence curve concept is independent of the underlying spatio-velocity phase space, i.e., the phase space can be substituted by a different model, which we demonstrate in Section 5.2.

2.1.2 Inertial Flow Maps and their Derivatives

The motion of inertial particles is governed by an ODE, such as Eq. (1) or Eq. (3). The *flow map* is a shortened notation, which maps a particle seeded at $(\mathbf{x},\mathbf{v},t)$ to its destination after pathline integration for duration τ. Following [28], we consider the m-D flow map of phase space $\hat{\mathbf{p}}$ as

$$\hat{\phi}(\mathbf{x},\mathbf{v},t,\tau) = \begin{pmatrix}\phi(\mathbf{x},\mathbf{v},t,\tau)\\\psi(\mathbf{x},\mathbf{v},t,\tau)\\t+\tau\end{pmatrix} \quad (5)$$

where ϕ denotes the location and ψ the velocity of an inertial particle after integration duration τ when starting the integration at location $\mathbf{x}$ at time t with initial velocity $\mathbf{v}$. Later, we require flow map derivatives of the inertial phase space. The gradient of $\hat{\phi}$ is an $m \times m$ matrix

$$\nabla\hat{\phi}(\mathbf{x},\mathbf{v},t,\tau) = \begin{pmatrix}\phi_{\mathbf{x}}(\mathbf{x},\mathbf{v},t,\tau) & \phi_{\mathbf{v}}(\mathbf{x},\mathbf{v},t,\tau) & \phi_t(\mathbf{x},\mathbf{v},t,\tau)\\\psi_{\mathbf{x}}(\mathbf{x},\mathbf{v},t,\tau) & \psi_{\mathbf{v}}(\mathbf{x},\mathbf{v},t,\tau) & \psi_t(\mathbf{x},\mathbf{v},t,\tau)\\\mathbf{0}_n^{\mathrm{T}} & \mathbf{0}_n^{\mathrm{T}} & 1\end{pmatrix} \quad (6)$$

where $\phi_{\mathbf{x}}$, $\phi_{\mathbf{v}}$, $\psi_{\mathbf{x}}$, $\psi_{\mathbf{v}}$ are $n \times n$ matrices describing the partial derivatives of $\hat{\phi}$ with respect to $\mathbf{x}$, $\mathbf{v}$, and ϕ_t, ψ_t being the start time partials.

2.2 Finite-Time Lyapunov Exponents

Lagrangian coherent structures are an established tool for the analysis of unsteady flows [30]. A frequently employed indicator for hyperbolic LCS is the finite-time Lyapunov exponent (FTLE) [60], which we formally introduce in the following for traditional tracer particles. Given is an unsteady vector field $\mathbf{u}(\mathbf{x},t)$. The *flow map* $\phi_t^\tau(\mathbf{x}) = \phi(\mathbf{x},t,\tau)$ maps a particle seeded at $(\mathbf{x},t)$ to its destination after pathline integration for duration τ. The (spatial) gradient of the flow map $\nabla\phi(\mathbf{x},t,\tau) = \frac{\partial}{\partial\mathbf{x}}\phi(\mathbf{x},t,\tau)$ describes the behavior of particles released close to each other. Hyperbolic LCS are defined as material surfaces that are locally separating the strongest, thus we are interested in the separation behavior of the nearby released particles, which is characterized by the right Cauchy-Green deformation tensor $\nabla^{\mathrm{T}}\nabla$. Its largest real eigenvalue $\lambda_{\max}$ denotes the (squared) largest magnitude of separation. Accounting for the exponential growth and normalizing by duration τ yields the finite-time Lyapunov exponent (FTLE) [29,32]:

$$\mathrm{FTLE}(\mathbf{x},t,\tau) = \frac{1}{|\tau|}\ln\sqrt{\lambda_{\max}(\nabla^{\mathrm{T}}\nabla)}, \quad (7)$$

In the literature, a variety of alternative LCS extraction techniques can be found (see [45] and [30] for an overview) that typically exploit differential properties of the flow map and/or Lagrangian properties of the flow around tracer trajectories. Haller and Yuan [29,32] proposed to release particles from a discrete grid and to compute the flow map gradient by finite differences of the reached particle destinations. This is the approach we used. The flow visualization community proposed alternative methods, such as localized FTLE [34], streak surface-based extraction [69] and timeline tracking [35]. A benchmark comparison of further computation methods was compiled by Kuhn et al. [36].

A number of acceleration strategies have been proposed to deliver faster FTLE computations, such as adaptive refinement of the flow map by Catmull-Rom interpolation [22], by the observation of filtered height ridges [56] or around automatically detected geometric structures [4]. Further, higher order flow map approximation [70], grid advection [57] and timeline refinement [35] schemes have been proposed. Generally, a number of integral curve approximation methods are available, such as hierarchical lines [33], interpolation [1,16] and edge maps [11], which can all be applied to accelerate the pathline integration. For interactive 3D FTLE visualizations, Barakat et al. [3] proposed a technique

that interleaves computation and rendering passes to view-dependently sample an adaptive hierarchical FTLE field representation. Recently, Machado et al. [39] extended streak-based topology to space-time bifurcation lines, which enables LCS extraction without FTLE. Günther et al. [24] applied unbiased free path sampling to generate high quality (ground truth) FTLE visualizations that are free of grid discretization and ray marching artifacts, though at higher computation cost.

2.3 Inertial Particles in Visualization

The analysis of inertial particle dynamics is a relatively young field in the visualization community. In an early work, Roettger et al. [54] determined the soiling of cars by visualizing particle concentrations via heat maps on the car surfaces. Günther et al. [23] simulated sand particle motion around a helicopter in slow forward flight close to a sediment bed. Using a flow map description, they defined inertial integral curves independent of the underlying equations of motion. Günther and Theisel [25] extracted Galilean-invariant vortex cores of swirling inertial particles by extending traditional vortex extractors that were originally devised for tracer particles to the m-D vector field in Eq. (1). Eventually, they reduced vortex extraction to an n-D parallel vectors problem. Later, they visualized the separation behavior of inertial particles that differ slightly in size [26]. For this, they defined a Lagrangian (i.e., integration-based) separation measure in the spirit of FTLE, but instead of a spatial flow map gradient, they consider the response time partial. Later in Section 5.3, we compute this measure in backward time. More recently, Günther and Theisel [27] conducted a full classification of the first-order critical points of the phase space $\hat{\mathbf{p}}$ in Eq. (1) for the 2D steady case. They also proposed an interactive glyph visualization that depicts the asymptotic behavior of inertial particles for varying initial positions and/or velocities.

Hyperbolic inertial Lagrangian coherent structures (ILCS) have been identified in [59] and [46] as ridges of a forward FTLE computation based on the trajectories of inertial particles. Raben et al. [51] computed FTLE for both tracer particles and inertial particles from experimental trajectories. Inertial FTLE was not only calculated based on spatial separation, but also on the separation in the spatio-velocity domain [21]. Sudharsan et al. [66] studied inertial forward FTLE for varying Stokes numbers St and density ratios R and indicated that forward IFTLE can serve as indicator for particle mixing (the fewer ridges, the better the mixing). They also studied the behavior of inertial particles in the context of massless tracer FTLE in backward time. They found that backward tracer FTLE ridges correlate with high aerosol particle concentration, whereas backward tracer FTLE valleys correspond to high bubble concentration. As we will show, the correspondence with tracer FTLE only holds for very light particles. We argue that a better correlation with preferential particle settling is found by LCS calculations based on backward trajectories of inertial particles. Direct inertial backward integration, however, is problematic in practice, as we review in the next section. A contribution of our paper is to study the preferential particle settling in the context of inertial backward FTLE, by applying and generalizing the recent influence curve concept.

2.4 Inertial Backward Integration

During forward integration, inertial particles tend to cluster. Formally, they are attracted by manifolds in the spatio-velocity domain [31,43]. Consequentially, a backward integration always has repelling behavior [27], which was illustrated in [28]. Haller and Sapsis [31] proposed the *inertial equation*, which is an ODE that allows to move on the attracting manifold in both forward and backward direction. However, their method cannot recover the initial velocity of a particle, and for larger particles, instabilities occur [59] that drive inertial particles away from the attracting manifold on which their method is valid. For their particle model, Sapsis and Haller [59] derived a threshold that characterizes when this happens, which they applied in [58]. In order to be able to calculate (approximating) backward inertial FTLE (attracting ILCS), Sapsis et al. [58] calculated ILCS in the context of jellyfish feeding, based on trajectories of the inertial equation. The inertial equation is an approximation. For neutrally buoyant particles in gravity-free environments, a leading-order approximation is simply the underlying vector
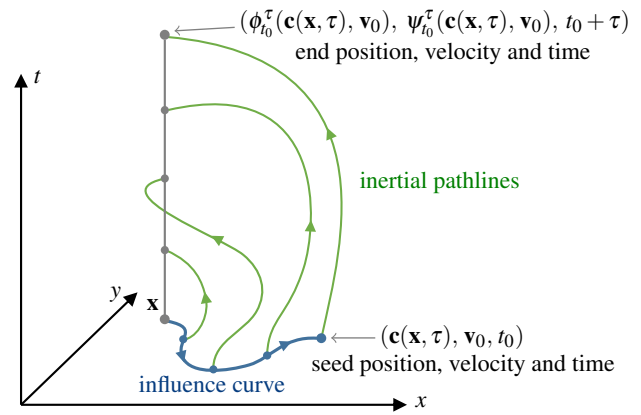

Fig. 2: Illustration of influence curve concept. The influence curve is the union of all spatial locations from which an inertial pathline integration (with initial velocity $\mathbf{v}_0$ and start time t_0) for duration τ reaches the observation point $\mathbf{x}$ (constant vertical line) at time $t_0 + \tau$. Note that the influence curve is computed per observation point $\mathbf{x}$ and that it is parameterized by the integration duration τ with which the returning inertial pathline is released from curve point $\mathbf{c}(\mathbf{x}, \tau)$. For massless particles, this illustration depicts a backward integrated streakline.

field $\mathbf{u}(\mathbf{x}, t)$, i.e., backward integration simply follows tracer particle trajectories. These trajectories have been shown to be not applicable to extract topological structures such as separatrices of inertial flow [27].

While direct backward integration of an inertial pathline is highly problematic, Günther and Theisel [28] proposed an alternative solution to integrate backward to a certain point in time. Instead of following an inertial pathline, they integrate *influence curves*, which are the inertial equivalent to a type of backward-integrated streakline. Influence curves can be computed as tangent curves of a derived vector field that is based on forward integrated flow map gradients only. In [28], these curves were defined for the phase space in Eq. (1). In the following section, we describe a generalization of the influence curve concept, which enables inertial backward integration in other phase spaces.

3 GENERALIZED INFLUENCE CURVES

Günther and Theisel [28] introduced the *influence curve* of an observation point $\mathbf{x}$ as a curve containing all points from which inertial integration with initial velocity $\mathbf{v}_0$ and start time t_0 ends in $\mathbf{x}$ after a certain integration duration τ. See Fig. 2 for an illustration. All influence curves can be defined as a family of parametric curves $\mathbf{c}(\mathbf{x}, \tau)$ so that

$$\phi(\mathbf{c}(\mathbf{x}, \tau), \mathbf{v}_0, t_0, \tau) = \mathbf{x} \qquad (8)$$

for all $\mathbf{x}$, curve parameterization τ and the family parameters $\mathbf{v}_0, t_0$.

The family of all influence curves can be characterized as pathlines of an n-dimensional unsteady vector field $\mathbf{h}(\mathbf{x}, t)$, starting at $t = t_0$:

$$\frac{d\mathbf{c}}{d\tau} = \mathbf{h}(\mathbf{c}(\mathbf{x}, \tau), t_0 + \tau). \qquad (9)$$

For a certain phase space $\hat{\mathbf{p}} = (\mathbf{p}^\mathbf{x}, \mathbf{p}^\mathbf{v}, 1)^\mathrm{T}$ in which particle trajectories arise as tangent curves, vector field $\mathbf{h}$ has a simple form:

$$\mathbf{h}(\mathbf{x}, t) = -\phi_\mathbf{x}^{-1} \left[\phi_\mathbf{v} \, \mathbf{p}^\mathbf{v}(\mathbf{x}, \mathbf{v}_0, t_0) + \phi_t \right] - \mathbf{p}^\mathbf{x}(\mathbf{x}, \mathbf{v}_0, t_0) \qquad (10)$$

where $\phi_\mathbf{x} = \phi_\mathbf{x}(\mathbf{x}, \mathbf{v}_0, t_0, t - t_0)$, $\phi_\mathbf{v} = \phi_\mathbf{v}(\mathbf{x}, \mathbf{v}_0, t_0, t - t_0)$ and $\phi_t = \phi_t(\mathbf{x}, \mathbf{v}_0, t_0, t - t_0)$ are inertial flow map derivatives that can be computed by forward integration, cf. Eq. (6). The expressions $\mathbf{p}^\mathbf{x}$ and $\mathbf{p}^\mathbf{v}$ denote the spatial and velocity subspace of the underlying phase space, respectively, in which inertial particle trajectories arise as tangent curves. With this, influence curves can be extracted via pathline integration in $\mathbf{h}$. The derivation of $\mathbf{h}$ follows an idea similar to the streakline vector field of Weinkauf and Theisel [72]. Given a point on the influence curve, $\mathbf{h}$ points in the direction, from where an inertial
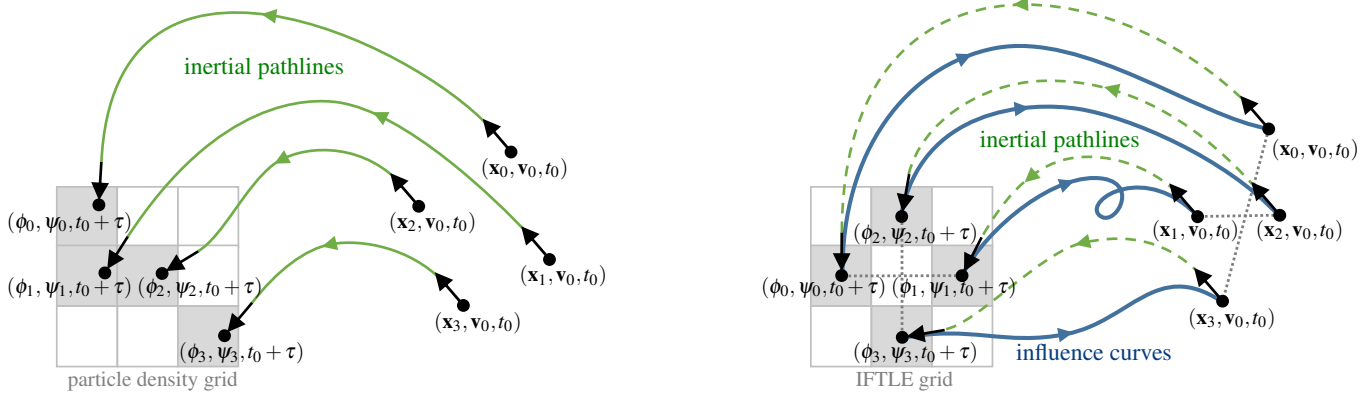
Fig. 3: Illustration of inertial particle settling (left) and inertial backward FTLE by the help of influence curves (right).

pathline will reach the observation as well, with the integration taking a little bit longer. The full derivation is in the appendix of [28].

Günther and Theisel [28] did not give the general form in Eq. (10), but inserted the phase space of Eq. (1) directly:

$$\mathbf{h}(\mathbf{x},t) = -\,\phi_{\mathbf{x}}^{-1}\left[\phi_{\mathbf{v}}\left(\frac{\mathbf{u}(\mathbf{x},t_0)-\mathbf{v}_0}{r}+\mathbf{g}\right)+\phi_t\right]-\mathbf{v}_0 \qquad (11)$$

Later in Section 5.2, we will compute influence curves in the phase space from Eq. (3). The corresponding influence curve vector field is:

$$\mathbf{h}(\mathbf{x},t) = -\,\phi_{\mathbf{x}}^{-1}\left[\phi_{\mathbf{v}}\left(\frac{R}{St}(\mathbf{u}(\mathbf{x},t_0)-\mathbf{v}_0)\right.\right.$$
$$\left.\left. +\frac{3R}{2}\frac{D\mathbf{u}(\mathbf{x},t_0)}{Dt}+(1-\frac{3R}{2})\mathbf{g}\right)+\phi_t\right]-\mathbf{v}_0 \quad (12)$$

In the following, we compute inertial backward FTLE in the influence curve vector field $\mathbf{h}(\mathbf{x},t)$.

4 INERTIAL BACKWARD FTLE AND PREFERENTIAL PARTICLE SETTLING

A central contribution of this paper is the insight that the preferential particle settling of inertial particles correlates with FTLE on the vector field $\mathbf{h}(\mathbf{x},t)$. Fig. 3 illustrates this correlation. Preferential particle settling is determined by releasing a large number of uniformly-distributed particles at time t_0 with a certain initial velocity $\mathbf{v}_0$, and observing where these particles arrive at time $t_0+\tau$. Then, the preferential settling is visualized by a particle density estimate, which reveals attracting structures. See Fig. 3 (left) for an illustration. The actual number of emitted particles is reported later in the individual result figures. Their transfer functions depict the particle density per unit area. In preferential particle settling, the initial velocity $\mathbf{v}_0$ is prescribed at time t_0 and is the same for all released inertial particles. Note that only inertial forward integration is involved in the computation.

Similarly, we would like to determine this attracting behavior by means of backward LCS, i.e., we intend to calculate inertial backward FTLE (IFTLE). As illustrated in Fig. 3 (right), we would like to compute IFTLE by taking finite differences of the reached location after inertial backward integration. But, not only is a direct inertial backward integration numerically infeasible [27, 28, 31, 66], we do not even know the velocity ψ_i with $i \in \{0,1,2,3\}$ with which the inertial backward integration would have to start from the observation ϕ_i. To obtain the same trajectories that were used in the preferential particle settling, we need to find trajectories that start with a known initial velocity $\mathbf{v}_0$ at time t_0 and lead to the respective observations ϕ_i at time $t_0+\tau$.

Using influence curves, we can recover where particles that where observed at time $t_0+\tau$ came from, *when released with a particular initial velocity* $\mathbf{v}_0$ *at time* t_0. Thus, we integrate influence curves in $\mathbf{h}(\mathbf{x},t)$ from ϕ_i to determine the sources $\mathbf{x}_i$. (The velocity ψ_i at the observation ϕ_i could now be determined by an inertial pathline integration from $\mathbf{x}_i$, since the trajectory will reach ϕ_i.) Since the $\mathbf{x}_i$ are the (theoretical)

end points of an inertial backward integration from ϕ_i with velocity ψ_i, and are at the same time the end points of the influence curves, we can calculate backward IFTLE directly on the vector field $\mathbf{h}(\mathbf{x},t)$, in which the influence curves appear as tangent curves. Fig. 1 gives an example for inertial backward FTLE by the use of influence curves in the vector field $\mathbf{h}(\mathbf{x},t)$ of Eq. (11). The ridges in the fields coincide and are in better agreement than the previously used backward FTLE on tracer particles [66], since the previous approach neglected inertia effects.

5 RESULTS AND DISCUSSION

In the following section, we present correlation results between inertial backward FTLE and preferential particle settling in five 2D and one 3D unsteady flow for the phase space in Eq. (1). Afterwards, we apply the phase space in Eq. (3) and demonstrate the computation of massless streaklines by the use of the influence curve framework. After demonstrating the applicability to other Lagrangian measures, we discuss the implementation and performance of our system. We close the section with a discussion of current limitations.

5.1 Inertial Backward FTLE

The results in this section are computed in the influence curve vector field in Eq. (11), i.e., they are based on the particle model in Eq. (1), as described by Crowe et al. [17].

5.1.1 Double Gyre

The DOUBLE GYRE [60] is a periodic 2D unsteady vector field that is commonly used as a benchmark for FTLE computations and was also used as primary example of inertial particle studies in the CFD literature [66]. In this paper, we define it in the temporal-periodic domain $D \times T = [0,2] \times [0,1] \times [0,10]$ and use the parameterization

$$\mathbf{u}(x,y,t) = \begin{pmatrix} -0.1\pi\sin(f(x,t)\pi)\cos(y\pi) \\ 0.1\pi\cos(f(x,t)\pi)\sin(y\pi)\frac{\mathrm{d}}{\mathrm{d}x}f(x,t) \end{pmatrix} \quad (13)$$

with $f(x,t) = a(t)x^2 + b(t)x$ and $a(t) = 0.25\sin(t\pi/5)$ and $b(t) = 1 - 0.5\sin(t\pi/5)$. Fig. 1 shows that FTLE on the influence curve vector field is in better agreement with the preferential particle settling than backward FTLE on tracer particles. Generally, we observe that inertial backward FTLE contains less ridge structures than FTLE on tracer particles, due to the inherent smoothing and damping by inertia. See the video for further results with varying particle sizes d_p.

5.1.2 Forced-Damped Duffing Oscillator

The FORCED-DAMPED DUFFING oscillator is a dynamical system that exhibits chaotic behavior. It has previously been used as a synthetic testing ground for observations of inertial particles [26]. The system can be described and visualized as unsteady 2D vector field of the form:

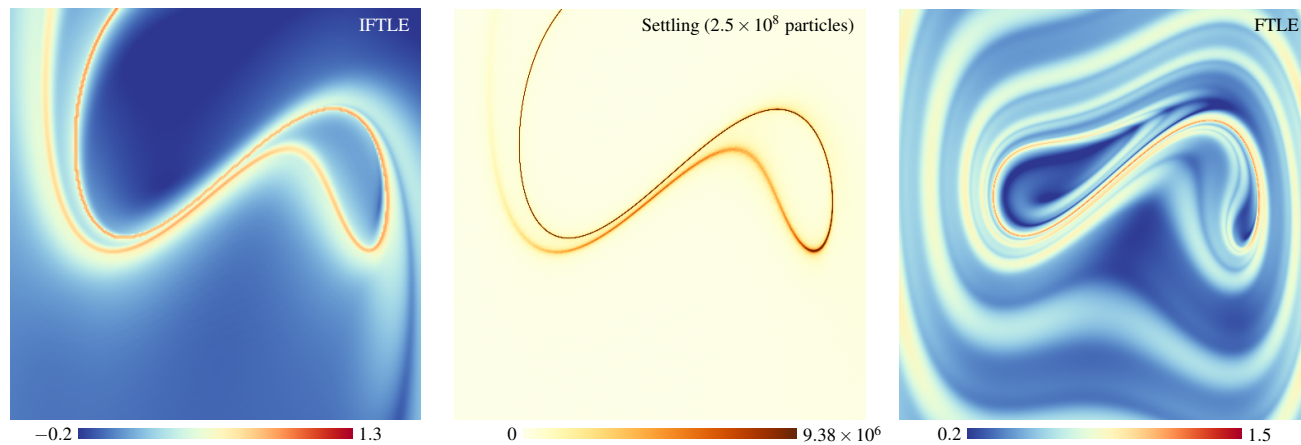$$\mathbf{u}(x,y,t) = \begin{pmatrix} y \\ x - x^3 - 0.25y + 0.4\cos t \end{pmatrix} \quad (14)$$

Fig. 4: Inertial backward FTLE (left, our method) and the preferential particle settling (center) correlate, whereas backward FTLE on tracer particles (right) contains not only more ridges (winding around the main structure), but the ridges are also deformed. Here, shown in the FORCED-DAMPED DUFFING, using Eq. (1) for $d_p = 200\,\mu m$, start time $t_0 = 0$ and integration duration $\tau = 7$.
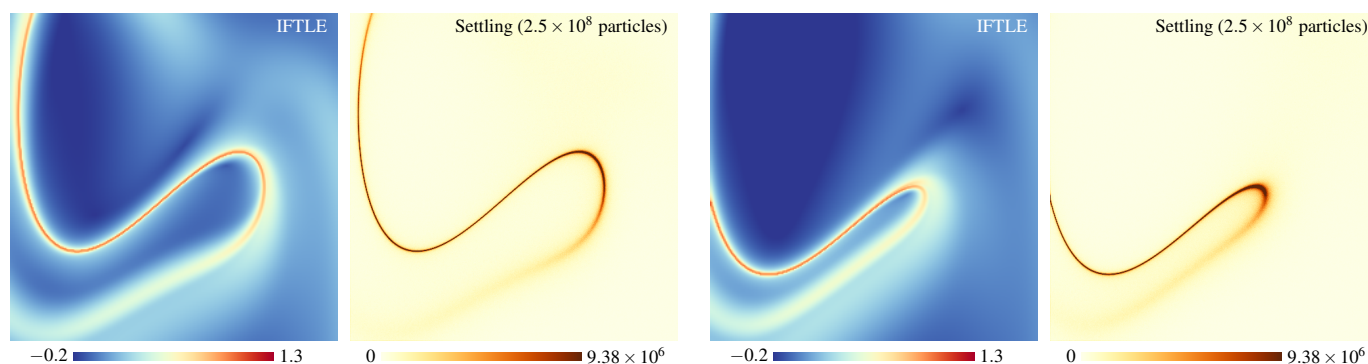

Fig. 5: Changing the initial velocity $\mathbf{v}_0$ has no effect on the attracting structures. Particle concentrations might change, depending on the seeding locations, but the overall attractors remain the same. In this example, we set $\mathbf{v}_0 = (1,0)^{\mathrm{T}}$, $d_p = 200\,\mu m$, $t_0 = 0$ and $\tau = 5$.

Fig. 6: Setting gravity to $\mathbf{g} = (0, -1)^{\mathrm{T}}$ changes the shape of the inertial particle attractor. Here, for $d_p = 200\,\mu m$, $t_0 = 0$ and $\tau = 5$. See Fig. 5 for the same setting without gravity.

here, in the spatial domain $D = [-2, 2]^2$. Fig. 4 depicts the flow for zero initial velocity and in a gravity-free environment. Evidently, the locations of IFTLE and FTLE ridges differ. In fact, in an animation over the response time, ridges "move" as shown in [26] for inertial forward FTLE. In this example here, backward tracer FTLE contains several more ridge structures that are winding around the central structure in the oscillator. As demonstrated, inertial backward FTLE correlates better with preferential particle settling.

In Fig. 5, we varied the initial velocity $\mathbf{v}_0$ of the inertial particles. Note that changing the initial velocity has no effect on the underlying phase space. Thus, it does not affect the attracting structures that inertial particles are drawn too. In fact, for sufficiently long integration time, the initial velocity has only little impact and particles cluster on the same structures, regardless of their initial velocities. Of course, the distributions might change, depending on the seeding locations, but the attractors are nevertheless the same.

Adding gravity, however, as in Fig. 6 does have an effect on the underlying phase space, as gravity is explicitly part of it. Thus, here, the structures in the preferential particle settling change and are also observed in the inertial backward FTLE field. Note that FTLE on tracer particles (see later Fig. 11 (right)) does not model gravity and would thus produce the same result for the settings in Figs. 5 and 6.

5.1.3   Square Cylinder Flow

The SQUARE CYLINDER flow [14] is a Navier-Stokes simulation of the 3D time-dependent flow around an obstacle. The uniformly resampled version of this vector field sequence was provided by Tino Weinkauf. Fig. 7 shows results of our inertial backward FTLE computation for the central 2D slice. Inertial particle dynamics are not bound by incompressibility and thus the largest eigenvalue of the Cauchy Green tensor

might become smaller than one, which results in a negative FTLE value. This can be seen at the vortex centers of the von Kármán vortex street. Due to inertia the particles are pushed away from the vortex cores and they cluster on the interfaces between the vortices. Backward FTLE on tracer particles, on the other hand, does not model these effects and suggests an increased particle concentration inside the vortices, which is incorrect.

5.1.4   Boussinesq Flow

The BOUSSINESQ flow is a 2D unsteady flow that was provided by Tino Weinkauf. The simulation is based on Gerris Flow solver [50] and uses the Boussinesq approximation to generate the turbulent vortex behavior. The domain contains a convection that develops around a heated cylinder. As shown in Fig. 8, this flow contains more vortices than the previous SQUARE CYLINDER flow, and therefore serves as more turbulent test case. The blocky grid artifacts were already present in the velocity data and stem from the adaptive simulation grid.

5.1.5   Helicopter in Forward Flight

The stirring of sand during helicopter takeoff and landing is under frequent investigation in the CFD community [37, 61, 67]. We use a validated airflow simulation [38] of a helicopter in slow forward flight close to the ground, which is courtesy of the aerodynamics group at Stuttgart University. This 3D data set was previously used in [23] in the context of inertial integral geometry. In Fig. 9, we examine a 2D slice of the domain in front of the helicopter. Of main interest is the vortex on the ground that is pushed forward by the helicopter, as it stirs up sand particles that enter the rotor disk, are convected with high speeds downward, and dislodge further sand particles when they hit the sediment bed. This chain reaction is called brown-out and leads to dangerous view limitations for the pilot. Inertial FTLE and particle
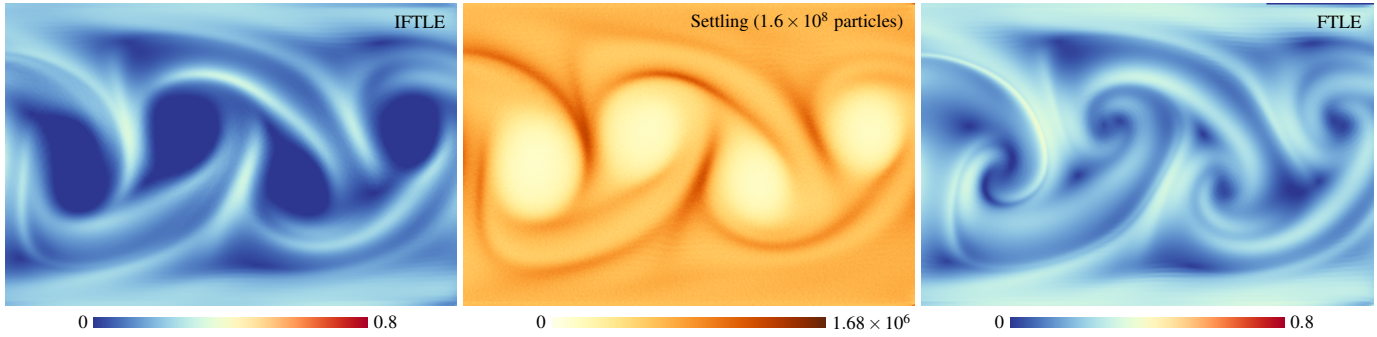
Fig. 7: Inertial backward FTLE (left, our method) and the preferential particle settling (center) reveal identical ridge structures. Backward FTLE on tracer particles (right) on the other hand, mistakenly indicates a presence of fine ridges inside the vortices. Here, shown in the SQUARE CYLINDER flow, using Eq. (1) for $d_p = 500\,\mu m$, start time $t_0 = 100$ and integration duration $\tau = 5$.
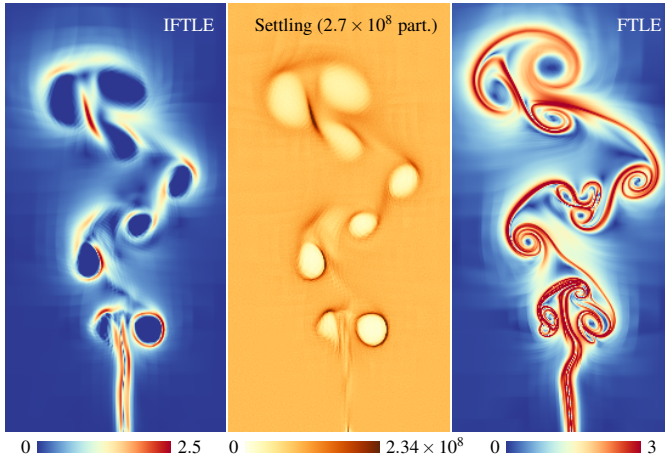

Fig. 8: Inertial backward FTLE (left, our method) and the preferential particle settling (center) not only correlate, but contain far less ridge structures than backward FTLE on tracer particles (right). Here, shown in the BOUSSINESQ flow, using Eq. (1) for $d_p = 200\,\mu m$, start time $t_0 = 5$ and integration duration $\tau = 0.7$.
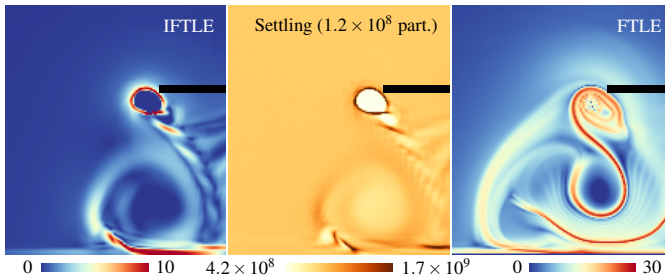

Fig. 9: Heavy particles in the HELICOPTER flow. A vortex forms at the tip of the rotor blade (black), trapping particles. Below is the main vortex. Here, using Eq. (1) for $d_p = 500\,\mu m$, duration $\tau = 0.15$.

settling show the uplift path and a potential particle trapping at the tip vortex at the blade. The dynamics of massless particles differ strongly.

5.1.6 Arnold-Beltrami-Childress Flow

Our approach naturally extends to the 3D case. In the next experiment, we used the following parameterization of the 3D unsteady Arnold-Beltrami-Childress (ABC) flow:

$$\mathbf{u}(x, y, z, t) = \begin{pmatrix} a(t)\,\sin(z) + c\,\cos(y) \\ b\,\sin(x) + a(t)\,\cos(z) \\ c\,\sin(y) + b\,\cos(x) \end{pmatrix} \quad (15)$$

with $a(t) = \sqrt{3} + (1 - e^{-0.1t})\sin(2\pi t)$, $b = \sqrt{2}$ and $c = 1$. The flow is defined in the domain $D \times T = [0, 2\pi]^3 \times [0, 2]$. In this flow, inertial particles cluster very quickly onto thin structures, thus we compare our

inertial backward FTLE with the preferential particle settling after integration duration $\tau = 1.5$ in Fig. 10. Backward FTLE on tracer particles, however, does not contain such thin structures, and the individual structures are not as connected as in the preferential particle settling. The parts of the structures that are visible, however, are close to the correct location. We used the visualization software Amira [64] to prepare the volume renderings. The employed resolution under-sampled the ridges, causing aliasing and stair case artifacts in Figs. 10 (a) and (b). A higher resolution would help, but would also increase the computation time.

5.2 Experiments in Other Phase Spaces

The generalization of the influence curve concept in Eq. (10) allows to compute influence curves in arbitrary spatio-velocity phase spaces. In the following, we use as phase space the equation of motion in Eq. (3). Afterwards, we apply the spatio-velocity phase space of a massless tracer particle, demonstrating the relation to massless flows.

5.2.1 Usage in More General Equations of Motion

The phase space in Eq. (3), as for instance used by Haller and Sapsis [31], describes inertial particle motion and thereby allows to specify a density ratio R between the particles and the surrounding medium, which enables buoyancy effects. In Fig. 11, we computed inertial backward FTLE based on influence curves defined over this phase space, i.e., Eq. (12), for aerosols with a small Stokes number. It can be seen that inertial backward FTLE and the preferential particle concentration correlate, whereas backward FTLE on tracer particles yields different structures. Evidently, FTLE on the influence curve field is the quantity that characterizes the asymptotic inertial particle behavior better. Upon experimenting with this particle model, however, we noticed numerical difficulties when increasing either the Stokes number or the density ratio. The computation of influence curves is integration-based and therefore subject to accumulating numerical errors. Numerical accuracy is an important topic for this work to which we devote Section 5.4.

5.2.2 Streakline Vector Field

Günther and Theisel gave the analogy that influence curves relate in the massless case to backward-integrated streaklines [28]. Thus, setting as phase space the tangent space of tracer particles (in the spatio-velocity domain) directly yields streaklines as tangent curves. Since influence curves evolve backward in time, we reverse the flow at time t_0 as $\tilde{\mathbf{u}}(\mathbf{x}, t) = -\mathbf{u}(\mathbf{x}, t_0 - (t - t_0))$ to eventually compute massless forward-integrated streaklines as influence curves in the phase space:

$$\hat{\mathbf{p}} = \frac{d}{dt}\begin{pmatrix} \mathbf{x} \\ \mathbf{v} \\ t \end{pmatrix} = \begin{pmatrix} \tilde{\mathbf{u}}(\mathbf{x}, t) \\ \tilde{\mathbf{a}}(\mathbf{x}, t) \\ 1 \end{pmatrix} \quad (16)$$

with $\tilde{\mathbf{a}}(\mathbf{x}, t) = \nabla\tilde{\mathbf{u}} \cdot \tilde{\mathbf{u}} + \tilde{\mathbf{u}}_t$ being the acceleration in the reversed flow.

Inserting the tracer phase space in Eq. (16) into the influence curve vector field in Eq. (10) yields

$$\mathbf{h}(\mathbf{x}, t) = -\phi_\mathbf{x}^{-1}\left[\phi_\mathbf{v}\,\tilde{\mathbf{a}}(\mathbf{x}, t_0) + \phi_t\right] - \tilde{\mathbf{u}}(\mathbf{x}, t_0). \quad (17)$$
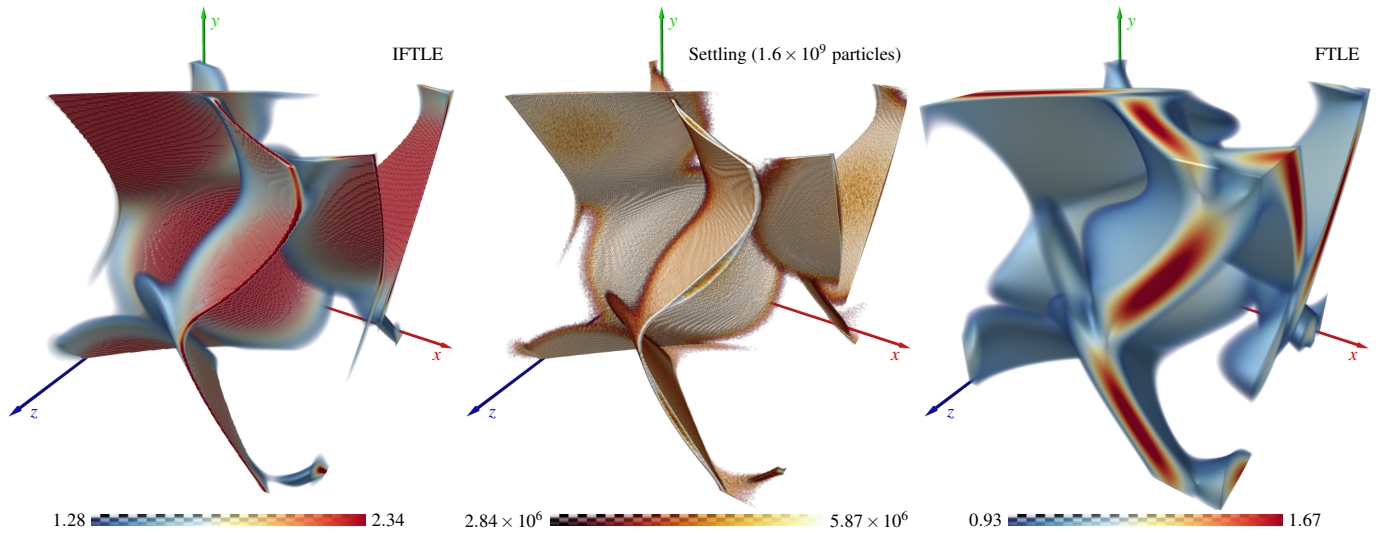
Fig. 10: A 3D example in the ABC flow. The ridges of inertial backward FTLE (left, our method) and the preferential particle settling (center) correlate, whereas backward FTLE on tracer particles (right) has less sharp structures that remain partially unconnected. Here, using Eq. (1) for $d_p = 250\,\mu m$, start time $t_0 = 0$ and integration duration $\tau = 1.5$.
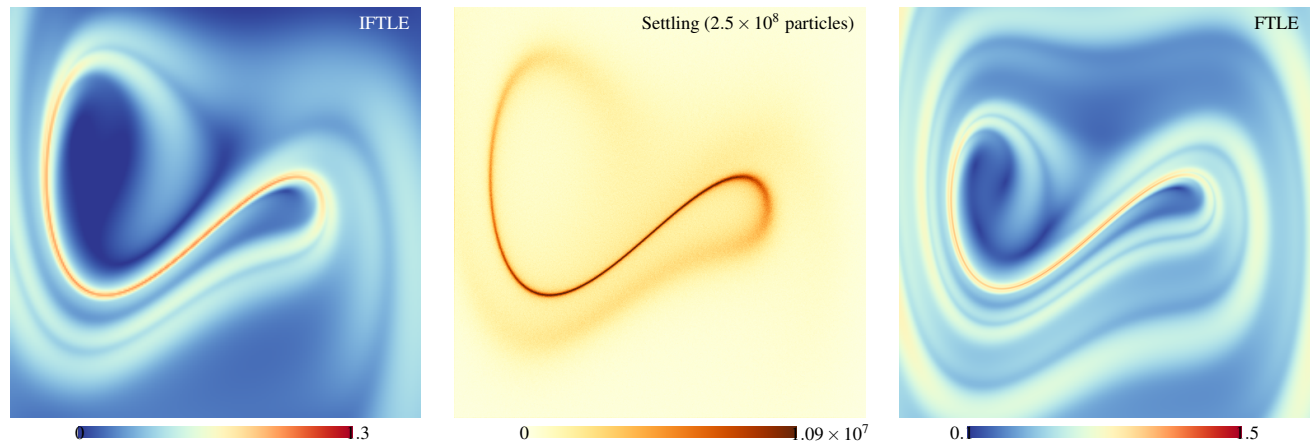

Fig. 11: Inertial backward FTLE (left, our method) and the preferential particle settling (center) are in agreement, whereas backward FTLE on tracer particles (right) differs visibly. Here, shown in the FORCED-DAMPED DUFFING, using Eq. (3) for density ratio $R = 0.1$ (aerosol), Stokes number $St = 0.01$, start time $t_0 = 0$ and integration duration $\tau = 5$.

Since the tracer phase space in Eq. (16) is independent of the current velocity state $\mathbf{v}$, the flow map derivative with respect to the velocity state is $\phi_{\mathbf{v}} = \mathbf{0}_{n \times n}$. Hence, Eq. (17) simplifies to

$$\mathbf{h}(\mathbf{x}, t) = -\phi_{\mathbf{x}}^{-1} \phi_t - \tilde{\mathbf{u}}(\mathbf{x}, t_0) \,. \tag{18}$$

That is, the acceleration $\tilde{\mathbf{a}}(\mathbf{x}, t)$ must not be evaluated as it vanishes.

Fig. 12 gives an example of streaklines obtained with Eq. (18). Here, streaklines were released in the SQUARE CYLINDER flow. The top halve of the image shows streaklines computed as tangent curves of the influence curve vector field $\mathbf{h}(\mathbf{x}, t)$ in Eq. (18), based on the tracer phase space in Eq. (16). The bottom halve shows ground truth streaklines computed from a fine temporally-resolved release of tracer particles from the seed points.

A few years ago, Weinkauf and Theisel [72] have shown that streak-lines can be computed as tangent curves of a derived vector field $\mathbf{w}$. Instead of defining a negated vector field $\tilde{\mathbf{u}}$ they used backward-integrated flow maps in $\mathbf{u}$, which we denote as $\tilde{\phi}$:

$$\mathbf{w} = \tilde{\phi}_{\mathbf{x}}^{-1} \cdot \tilde{\phi}_t + \mathbf{u}(\mathbf{x}, t_0) \,. \tag{19}$$

Note that backward integration (rather than reversing the flow) flips the sign of the temporal derivative of the flow map $\tilde{\phi}_t = -\phi_t$ and that $\mathbf{u}(\mathbf{x}, t_0) = -\tilde{\mathbf{u}}(\mathbf{x}, t_0)$. Hence, Eq. (18) can be directly turned into Eq. (19). In retrospect, the fact that streakline vector fields [72] and
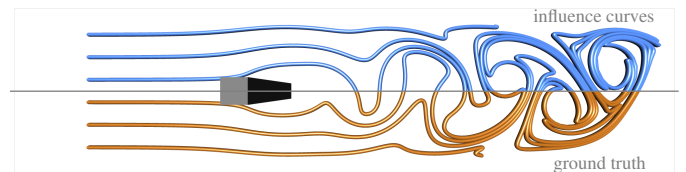

Fig. 12: Streaklines as tangent curves of the influence curve vector field, defined on a tracer phase space (top), and as a ground truth computed by traditional particle advection (bottom), with $t_0 = 75$ and $\tau = 40$.

influence curve vector fields [28] turn out to relate to each other is not surprising, since their respective construction followed a similar path.

5.3 Experiments with Other Lagrangian Measures

In the following, we demonstrate that influence curves are even more versatile and can also be used to compute other inertial Lagrangian measures in backward time. We will focus on the two Lagrangian measures: finite-time mass separation (FTMS) [26] and accumulated curvature. For both, we use influence curves in $\mathbf{h}(\mathbf{x}, t)$ from Eq. (11).

5.3.1 Finite-Time Mass Separation

Finite-time mass separation is a scalar field that was proposed by Günther and Theisel [26] in forward time. It is used to study the separation of inertial particles that were released from the same location,
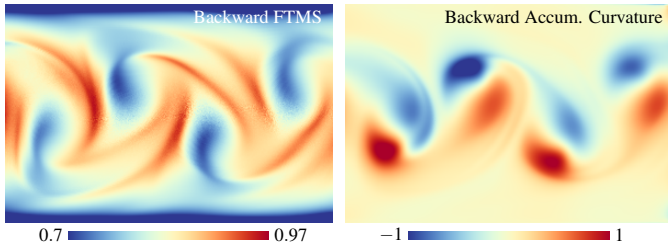
Fig. 13: Other Lagrangian measures in backward time: finite-time mass separation (FTMS) [26] (left) and accumulated curvature (right) in the SQUARE CYLINDER flow with $d_p = 500\,\mu m$, $t_0 = 100$ and $\tau = 5$.

but with slightly different mass. The measure computes the response time partial of the inertial flow map and normalizes it in the spirit of FTLE (accounting for logarithmic growth and integration duration):

$$\text{FTMS}(\mathbf{x}, \mathbf{v}_0, t, \tau, r) = \frac{1}{|\tau|} \ln \left\| \frac{d\phi(\mathbf{x}, \mathbf{v}_0, t, \tau, r)}{dr} \right\|. \qquad (20)$$

While in the previous inertial flow map definition of Section 2.1.2, the response time r was neglected for brevity, we explicitly write it here as a parameter of the inertial flow map in order to formally define its derivative. An example of the FTMS field is shown in Fig. 13 (left). Forward FTMS calculates the rate at which differently-sized inertial particles separate. Backward FTMS on the other hand characterizes how fast differently-sized inertial particles are attracted toward the *same* structure. This is interesting, since attractors of inertial particles are usually dependent on the response time, yet we can see that in some areas attractors correlate. We believe that studying the reasons for these correlations could be an interesting topic for future work.

5.3.2 Accumulated Curvature of Influence Curves

In the following, we depict the accumulated curvature of the influence curves $\mathbf{c}(\mathbf{x}, t)$. We consider only the 2D case for which the signed curvature of the influence curve is defined as

$$\kappa(\mathbf{x}, t) = \frac{\det\left[\mathbf{h}(\mathbf{c}(\mathbf{x}, t), t_0 + t), \frac{d\mathbf{h}(\mathbf{c}(\mathbf{x}, t), t_0 + t)}{dt} \right]}{\| \mathbf{h}(\mathbf{c}(\mathbf{x}, t), t_0 + t) \|^3}. \qquad (21)$$

The numerator computes the determinant of a 2×2 matrix containing in the columns the first and second order time partials of the curve, i.e., the influence curve vector field $\mathbf{h}$ itself and its temporal derivative. In 3D, curvature can be defined similarly, though without sign. The accumulated curvature $K(\mathbf{x}, t)$ becomes:

$$K(\mathbf{x}, t) = \int_0^t \kappa(\mathbf{x}, s)\, ds \qquad (22)$$

Fig. 13 (right) gives an example. In the SQUARE CYLINDER flow, streaklines work very well in the massless case to reveal the von Kármán vortex street (see Fig. 12), as the curves themselves and their geometric properties align with the vortex structures. In the inertial case, we use the equivalent to streaklines, i.e., we visualize the accumulated curvature of an influence curve at its seed point. The vortices are revealed and the bending direction of the influence curves (left or right) becomes apparent by the sign.

5.4 Implementation and Performance

For all measurements throughout the paper, we used an Intel Core i7-2600K CPU with 3.4 GHz. Table 1 reports the computation time, image resolutions and average residual errors for the data sets shown throughout the paper. The FORCED-DAMPED DUFFING in Fig. 11 was computed faster than in Fig. 4 due to shorter integration time τ.

Günther and Theisel [28] have shown that the influence curve vector field might exhibit strong variations in its magnitude and that thus an adaptive numerical integration is mandatory. Similar to them, we used the Runge-Kutta-Fehlberg (RK45) method. Since inertial particles that were released from an influence curve should reach the observation

Data set	Figure	Resolution	Time	Residual
DOUBLE GYRE	Fig. 1	800×400	5.3	2.1×10^{-7}
FORCED DUFFING	Fig. 4	250×250	4.2	5.0×10^{-8}
SQUARE CYLINDER	Fig. 7	300×200	1.4	1.7×10^{-7}
BOUSSINESQ	Fig. 8	300×900	1.2	2.0×10^{-10}
HELICOPTER	Fig. 9	150×180	0.2	1.0×10^{-10}
ABC	Fig. 10	$200 \times 200 \times 200$	7.8	3.0×10^{-10}
FORCED DUFFING	Fig. 11	250×250	1.2	1.5×10^{-8}

Table 1: Total extraction time (in hours) of influence curves in the shown figures, the used grid resolutions and the average residual error.
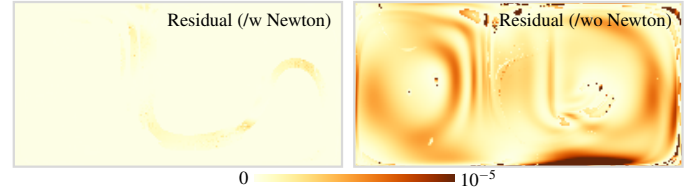

Fig. 14: Error plots for the influence curve computation with and without subsequent Newton iterations for refinement in the DOUBLE GYRE with $d_p = 200\,\mu m$, $t_0 = 0$ and $\tau = 9$. Visually, both corresponding IFTLE visualizations look similar to Fig. 1.

exactly, Newton iterations can be applied to further minimize the deviation [28]. Adaptive integrators require a user-specified error tolerance to be set, which guides the adjustment of the step size. Thereby, a trade-off is made between accuracy and speed.

Since integration in $\mathbf{h}(\mathbf{x}, t)$ becomes numerically more difficult with increasing integration duration τ [28], the setting of the error tolerance is dependent on τ. To determine the error tolerance automatically, we use an iterative adjustment. We start with a high error tolerance, meaning that the adaptive RK45 integrator does not decrease step sizes too strongly. If the total accumulated error cannot be removed by subsequent Newton iterations, we restart the experiment with a lower error tolerance (reduced by factor $1/10$), until the residual error is sufficiently small ($< 10^{-7}$) or a maximum number of attempts is reached. Table 2 lists performance statistics of this procedure in the DOUBLE GYRE for varying τ. In particular, we list the average time an influence curve integration takes dependent on the required number of adjustment iterations (attempts). Further, we list the percentage of influence curves that were computed with the respective number of adjustment iterations. It can be seen that the computation time grows quickly with increasing τ. More importantly, for higher τ the number of adjustment iterations increases. Evidently, the numerical computation becomes more involved. In fact, the residual error cannot be reduced below the threshold for all influence curves when using only 4 attempts, which can be seen by the increasing number of curves reaching the last attempt, and by the growing average residual, which exceeds the desired threshold of 10^{-7}. Nevertheless, in this experiment, the residual errors stayed for all integration durations below 10^{-5}.

The adaptive adjustment of the error tolerance generates an overhead. If the optimal error tolerance is known a-priori and used instead, the computation time in the DOUBLE GYRE can be reduced to about 76%. In the other data sets, the overhead was much smaller, since the majority of the curves could be computed in earlier attempts.

Fig. 14 depicts the impact of the subsequent Newton iterations. Not only does the refinement reduce the residual error, it also accelerates the computation since early attempts with a too coarse error tolerance might be correctable, hence avoiding a restart of the influence curve integration with a lower error tolerance. In the DOUBLE GYRE example with a resolution of 200×100, the computation time is reduced by Newton iterations from $83\,min$ to $34\,min$.

5.5 Limitations

Influence curves are described as tangent curves, and thus they are subject to accumulating numerical errors. We approached this problem with an adaptive integrator and an iterative reduction of its error tolerance. Decreasing the error tolerance and step sizes increases the computation time significantly and thus becomes quickly infeasible for

duration	1 iteration		2 iterations		3 iterations		4 iterations		total	residual
τ	avg. time	done (%)	avg. time	done (%)	avg. time	done (%)	avg. time	done (%)	time	avg. error
1	3.46	88.8	9.01	9.2	15.38	1.3	25.12	0.7	3.2 *sec*	0.94×10^{-7}
2	10.26	80.6	20.99	12.9	49.1	2.6	105.99	3.9	10.8 *sec*	0.95×10^{-7}
4	33.41	68.8	119.98	16.2	189.81	5.6	289.09	9.4	50.8 *sec*	1.08×10^{-7}
6	81.04	59.4	184.36	21.9	366.53	9.2	737.28	9.5	2.00 *min*	1.06×10^{-7}
8	185.79	59.2	372.85	15.5	632.25	8.5	1,164.96	16.8	4.36 *min*	1.33×10^{-7}
10	304.03	46.1	575.35	24.9	1,079.38	11.1	2,016.48	17.9	7.96 *min*	1.32×10^{-7}
12	411.38	36.5	1,111.53	24.1	1,960.18	11.1	5,812.99	28.3	24.07 *min*	2.41×10^{-7}

Table 2: Timings of the numerical influence curve integration for varying durations τ in the DOUBLE GYRE at 100×50 pixels with $d_p = 200\,\mu m$ and $t_0 = 0$. Our method iteratively decreases the error tolerance until a solution with sufficiently small error is found. Here, the average influence curve computation time (in *msec*) is listed for the respective number of iterations they required, along with the number of influence curves in each category (in %). The last two columns list the total time required to compute an influence curve for every pixel as well as average residual errors.
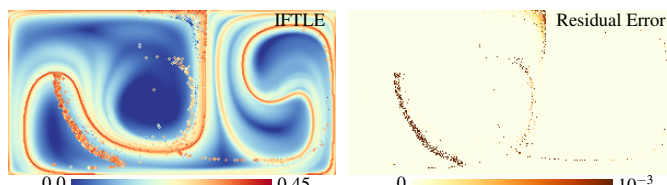

Fig. 15: For $\tau = 14$ with insufficiently small step size, the residual error of the influence curves is quite high. For several pixels the residual cannot be removed with subsequent Newton iterations, thus the IFTLE image contains visible artifacts. Here, with $d_p = 200\,\mu m$ and $t_0 = 0$.

higher integration durations τ. Due to numerical limits, it might not even be possible to reduce the residual error below a desired threshold for high τ, which is a general limitation of influence curves. Hence, we focused on moderate integration durations. Increasing integration durations further, or experimenting in Eq. 12 with higher density ratios R or Stokes numbers St led to numerical issues that could not be eliminated in feasible computation time. Fig. 15 demonstrates a failure case.

Further, influence curve integration stops at domain boundaries, even though curves might reenter the domain. We inherit this limitation from [28], who suggested a search for reentry points for future work.

Due to numerical errors, the extracted influence curves might jitter. The variation is in the order of the residual, which we set by default to 10^{-7}. Only in Fig. 13, the residual was set to 10^{-5} to trade quality for shorter computation time, though this results in visible noise artifacts. The theoretically more elegant solution is to recompute with higher accuracy, though a practical (and most likely faster) solution might be to remove these artifacts in a post-process, e.g., by enforcing spatial smoothness on the recovered sources. We would like to investigate such post-processing in the future.

6 CONCLUSION

In this paper, we generalized the influence curve concept of [28] to general equations of motion in the spatio-velocity-time domain. Based on this, we computed the sources of dispersed pollutants that were advected by the models described in Crowe et al. [17] and Haller and Sapsis [31]. We applied the concept to extend the recent work of Sudharsan et al. [66], who studied the relation between preferential particle settling of inertial particles and backward FTLE on tracer particles. We have demonstrated that the usage of the (generalized) influence curve concept to compute inertial backward FTLE (IFTLE) is in better agreement with preferential particle settling. Further, we have shown that an influence curve vector field based on a tracer phase space emits streaklines as tangent curves, which connects to the work of Weinkauf and Theisel [72]. Our results have revealed that inertial backward FTLE is the right measure, but that influence curves tend to numerical difficulties when integrating far backward in time.

In the future, we would like to investigate how this could be stabilized and whether other constructions are possible. In this work, we have shown the potential of influence curves, including applications to other Lagrangian measures, such as FTMS and accumulated curvature. We would like to apply the idea to other backward integration related approaches that have previously been unavailable for inertial particles.

REFERENCES

[1] A. Agranovsky, H. Obermaier, C. Garth, and K. I. Joy. A multi-resolution interpolation scheme for pathline based Lagrangian flow representations. In *Proc. SPIE, Visual Data Analysis Conference*, 2015.

[2] A. Babiano, J. H. E. Cartwright, O. Piro, and A. Provenzale. Dynamics of a small neutrally buoyant sphere in a fluid and targeting in Hamiltonian systems. *Phys. Rev. Lett.*, 84:5764–5767, Jun 2000.

[3] S. S. Barakat, C. Garth, and X. Tricoche. Interactive computation and rendering of finite-time Lyapunov exponent fields. *IEEE Transactions on Visualization and Computer Graphics*, 18(8):1368–1380, 2012.

[4] S. S. Barakat and X. Tricoche. Adaptive refinement of the flow map using sparse samples. *IEEE TVCG (Proc. SciVis)*, 19(12):2753–2762, 2013.

[5] J. Bec. Fractal clustering of inertial particles in random flows. *Physics of Fluids*, 15(11):L81–L84, 2003.

[6] J. Bec, L. Biferale, M. Cencini, A. Lanotte, S. Musacchio, and F. Toschi. Heavy particle concentration in turbulence at dissipative and inertial scales. *Phys. Rev. Lett.*, 98:084502, 2007.

[7] J. Bec, L. Biferale, M. Cencini, A. S. Lanotte, and F. Toschi. Spatial and velocity statistics of inertial particles in turbulent flows. *Journal of Physics: Conference Series*, 333(1):012003, 2011.

[8] J. Bec, A. Celani, M. Cencini, and S. Musacchio. Clustering and collisions of heavy particles in random smooth flows. *Physics of Fluids*, 17(7):073301, 2005.

[9] I. J. Benczik, Z. Toroczkai, and T. Tél. Selective sensitivity of open chaotic flows on inertial tracer advection: Catching particles with a stick. *Phys. Rev. Lett.*, 89:164501, Sep 2002.

[10] R. Benzi, L. Biferale, E. Calzavarini, D. Lohse, and F. Toschi. Velocity-gradient statistics along particle trajectories in turbulent flows: The refined similarity hypothesis in the Lagrangian frame. *Phys. Rev. E*, 80:066318, Dec 2009.

[11] H. Bhatia, S. Jadhav, P.-T. Bremer, G. Chen, J. A. Levine, L. G. Nonato, and V. Pascucci. Flow visualization with quantified spatial and temporal errors using edge maps. *IEEE TVCG*, 18(9):1383–1396, 2012.

[12] R. Bordás. *Optical measurements in disperse two-phase flows: Application to rain formation in cumulus clouds*. PhD thesis, Univ. Magdeburg, 2011.

[13] J. K. M. Brown and M. S. Hovmøller. Aerial dispersal of pathogens on the global and continental scales and its impact on plant disease. *Science*, 297(5581):537–541, 2002.

[14] S. Camarri, M.-V. Salvetti, M. Buffoni, and A. Iollo. Simulation of the three-dimensional flow around a square cylinder between parallel walls at moderate Reynolds numbers. In *XVII Congresso di Meccanica Teorica ed Applicata*, 2005.

[15] C. M. Casciola, P. Gualtieri, F. Picano, G. Sardina, and G. Troiani. Dynamics of inertial particles in free jets. *Physica Scripta*, 2010(T142):014001, 2010.

[16] J. Chandler, H. Obermaier, and K. I. Joy. Interpolation-based pathline tracing in particle-based flow visualization. *IEEE Transactions on Visualization and Computer Graphics*, 21(1):68–80, 2015.

[17] C. Crowe, M. Sommerfield, and Y. Tsuji. *Multiphase Flows with Droplets and Particles*. CRC Press, 1998.

[18] J. K. Eaton and J. R. Fessler. Preferential concentration of particles by turbulence. *International Journal of Multiphase Flow*, 20:169–209, 1994.

[19] A. Espinosa-Gayosso, M. Ghisalberti, G. N. Ivey, and N. L. Jones. Density-ratio effects on the capture of suspended particles in aquatic systems. *Journal of Fluid Mechanics*, 783:191–210, 11 2015.

[20] M. Farazmand and G. Haller. The Maxey–Riley equation: Existence, uniqueness and regularity of solutions. *Nonlinear Analysis: Real World Applications*, 22:98–106, 2015.

[21] D. Garaboa-Paz and V. Pérez-Muñuzuri. A method to calculate finite-time Lyapunov exponents for inertial particles in incompressible flows. *Nonlinear Processes in Geophysics*, 22(5):571–577, 2015.

[22] C. Garth, F. Gerhardt, X. Tricoche, and H. Hagen. Efficient computation and visualization of coherent structures in fluid flow applications. *IEEE TVCG (Proc. IEEE Visualization)*, 13(6):1464–1471, 2007.

[23] T. Günther, A. Kuhn, B. Kutz, and H. Theisel. Mass-dependent integral curves in unsteady vector fields. *Computer Graphics Forum (Proc. EuroVis)*, 32(3):211–220, 2013.

[24] T. Günther, A. Kuhn, and H. Theisel. MCFTLE: Monte Carlo rendering of finite-time Lyapunov exponent fields. *Computer Graphics Forum (Proc. EuroVis)*, 35(3):to appear, 2016.

[25] T. Günther and H. Theisel. Vortex cores of inertial particles. *IEEE Trans. on Visualization and Computer Graphics (Proc. IEEE Scientific Visualization)*, 20(12):2535–2544, 2014.

[26] T. Günther and H. Theisel. Finite-time mass separation for comparative visualizations of inertial particles. *Computer Graphics Forum (Proc. EuroVis)*, 34(3):471–480, 2015.

[27] T. Günther and H. Theisel. Inertial steady 2D vector field topology. *Computer Graphics Forum (Proc. Eurographics)*, 35(2):455–466, 2016.

[28] T. Günther and H. Theisel. Source inversion by forward integration in inertial flows. *CGF (Proc. EuroVis)*, 35(3):to appear, 2016.

[29] G. Haller. Distinguished material surfaces and coherent structures in three-dimensional fluid flows. *Physica D: Nonlinear Phenomena*, 149(4):248–277, Mar. 2001.

[30] G. Haller. Lagrangian coherent structures. *Annual Review of Fluid Mechanics*, 47:137–162, 2015.

[31] G. Haller and T. Sapsis. Where do inertial particles go in fluid flows? *Physica D: Nonlinear Phenomena*, 237:573–583, May 2008.

[32] G. Haller and G. Yuan. Lagrangian coherent structures and mixing in two-dimensional turbulence. *Physica D: Nonlinear Phenomena*, 147(3–4):352–370, 2000.

[33] M. Hlawatsch, F. Sadlo, and D. Weiskopf. Hierarchical line integration. *IEEE Trans. on Vis. and Computer Graphics*, 17(8):1148–1163, 2011.

[34] J. Kasten, C. Petz, I. Hotz, B. Noack, and H.-C. Hege. Localized finite-time Lyapunov exponent for unsteady flow analysis. In *Proceedings of Vision, Modeling and Visualization*, pages 265–274, 2009.

[35] A. Kuhn, W. Engelke, C. Rössl, M. Hadwiger, and H. Theisel. Time line cell tracking for the approximation of Lagrangian coherent structures with subgrid accuracy. *Computer Graphics Forum*, 33(1):222–234, 2014.

[36] A. Kuhn, C. Rössl, T. Weinkauf, and H. Theisel. A benchmark for evaluating FTLE computations. In *Proceedings of 5th IEEE Pacific Visualization Symposium (PacificVis 2012)*, pages 121–128, Songdo, Korea, 2012.

[37] B. M. Kutz, T. Günther, A. Rumpf, and A. Kuhn. Numerical examination of a model rotor in brownout conditions. In *Proceedings of the American Helicopter Society*, number AHS2014-000343, 2014.

[38] B. M. Kutz, U. Kowarsch, M. Kessler, and E. Krämer. Numerical investigation of helicopter rotors in ground effect. In *30th AIAA Applied Aerodynamics Conference*, 2012.

[39] G. M. Machado, S. Boblest, T. Ertl, and F. Sadlo. Space-time bifurcation lines for extraction of 2D Lagrangian coherent structures. *Computer Graphics Forum (Proc. EuroVis)*, 35(3):to appear, 2016.

[40] M. R. Maxey. The gravitational settling of aerosol particles in homogeneous turbulence and random flow fields. *Journal of Fluid Mechanics*, 174:441–465, 1987.

[41] M. R. Maxey. The motion of small spherical particles in a cellular flow field. *Physics of Fluids*, 30(7):1915–1928, 1987.

[42] M. R. Maxey and J. J. Riley. Equation of motion for a small rigid sphere in a nonuniform flow. *Physics of Fluids*, 26(4):883–889, 1983.

[43] E. Mograbi and E. Bar-Ziv. On the asymptotic solution of the Maxey-Riley equation. *Physics of Fluids*, 18(5), 2006.

[44] D. F. S. Natusch, J. R. Wallace, and C. A. Evans. Toxic trace elements: Preferential concentration in respirable particles. *Science*, 183(4121):202–204, 1974.

[45] K. Onu, F. Huhn, and G. Haller. LCS tool: a computational platform for Lagrangian coherent structures. *Journal of Computational Science*, 7:26–36, 2015.

[46] J. Peng and J. O. Dabiri. Transport of inertial particles by Lagrangian coherent structures: Application to predator–prey interaction in jellyfish feeding. *Journal of Fluid Mechanics*, 623:75–84, 3 2009.

[47] V. Pérez-Muñuzuri and D. Garaboa-Paz. Mixing of spherical bubbles with time-dependent radius in incompressible flows. *Phys. Rev. E*, 93:023107, 2016.

[48] F. Picano, G. Sardina, P. Gualtieri, and C. Casciola. DNS of a free turbulent jet laden with small inertial particles. In H. Kuerten, B. Geurts, V. Armenio, and J. Fröhlich, editors, *Direct and Large-Eddy Simulation VIII*, volume 15 of *ERCOFTAC Series*, pages 189–194. Springer Netherlands, 2011.

[49] S.-D. Poisson. *Mémoire sur les équations générales de l'équilibre et du mouvement des corps solides élastiques et des fluides: lu à l'Académie des sciences le 12 octobre 1829*. De l'Imprimerie royale, 1831.

[50] S. Popinet. Free computational fluid dynamics. *Cluster World 2*, (6), 2004.

[51] S. G. Raben, S. D. Ross, and P. P. Vlachos. Experimental determination of three-dimensional finite-time Lyapunov exponents in multi-component flows. *Experiments in Fluids*, 55(10):1–6, 2014.

[52] S. Ravichandran and R. Govindarajan. Caustics and clustering in the vicinity of a vortex. *Physics of Fluids*, 27(3):033305, 2015.

[53] J. J. Riley and G. S. Patterson. Diffusion experiments with numerically integrated isotropic turbulence. *Physics of Fluids*, 17(2):292–297, 1974.

[54] S. Roettger, M. Schulz, W. Bartelheimer, and T. Ertl. Automotive soiling simulation based on massive particle tracing. In *Data Visualization 2001*, Eurographics, pages 309–317. Springer Vienna, 2001.

[55] J. Rubin, C. K. R. T. Jones, and M. Maxey. Settling and asymptotic motion of aerosol particles in a cellular flow field. *Journal of Nonlinear Science*, 5(4):337–358, 1995.

[56] F. Sadlo and R. Peikert. Efficient visualization of Lagrangian coherent structures by filtered AMR ridge extraction. *IEEE Trans. on Visualization and Computer Graphics (IEEE Visualization)*, 13(6):1456–1463, 2007.

[57] F. Sadlo, A. Rigazzi, and R. Peikert. Time-dependent visualization of Lagrangian coherent structures by grid advection. In *Topo. Methods in Data Analysis and Vis.*, pages 151–165. Springer Berlin Heidelberg, 2011.

[58] T. Sapsis, J. Peng, and G. Haller. Instabilities on prey dynamics in jellyfish feeding. *Bull Math Biol.*, 73(8):1841–1856, 2011.

[59] T. P. Sapsis and G. Haller. Inertial particle dynamics in a hurricane. *Journal of the Atmospheric Sciences*, 2009.

[60] S. C. Shadden, F. Lekien, and J. E. Marsden. Definition and properties of Lagrangian coherent structures from finite-time Lyapunov exponents in two-dimensional aperiodic flows. *Physica D: Nonlinear Phenomena*, 212(3-4):271–304, 2005.

[61] Y. Shao and A. Li. Numerical modelling of saltation in the atmospheric surface layer. *Boundary-Layer Meteorology*, 91:199–225, 1999.

[62] R. A. Shaw, W. C. Reade, L. R. Collins, and J. Verlinde. Preferential concentration of cloud droplets by turbulence: Effects on the early evolution of cumulus cloud droplet spectra. *Journal of the Atmospheric Sciences*, 55(11):1965–1976, 1998.

[63] K. D. Squires and J. K. Eaton. Preferential concentration of particles by turbulence. *Physics of Fluids A*, 3(5):1169–1178, 1991.

[64] D. Stalling, M. Westerhoff, and H.-C. Hege. Amira: A highly interactive system for visual data analysis. In *The Visualization Handbook*, pages 749–767. Elsevier, 2005.

[65] H. Stommel. Trajectories of small bodies sinking slowly through convection cells. *J. mar. Res*, 8(11):24–29, 1949.

[66] M. Sudharsan, S. L. Brunton, and J. J. Riley. Lagrangian coherent structures and inertial particle dynamics. *ArXiv e-prints*, 2015. 1512.05733.

[67] M. Syal, B. Govindarajan, and J. G. Leishman. Mesoscale sediment tracking methodology to analyze brownout cloud developments. In *Proceedings of the American Helicopter Society, 66th Annual Forum*, 2010.

[68] W. Tang, B. Knutson, A. Mahalov, and R. Dimitrova. The geometry of inertial particle mixing in urban flows, from deterministic and random displacement models. *Physics of Fluids*, 24(6):063302, 2012.

[69] M. Üffinger, F. Sadlo, and T. Ertl. A time-dependent vector field topology based on streak surfaces. *IEEE TVCG*, 19(3):379–392, 2013.

[70] M. Üffinger, F. Sadlo, M. Kirby, C. Hansen, and T. Ertl. FTLE computation beyond first-order approximation. In *Eurographics (Short Papers)*, pages 61–64, 2012.

[71] R. D. Vilela, A. P. S. de Moura, and C. Grebogi. Finite-size effects on open chaotic advection. *Phys. Rev. E*, 73:026302, 2006.

[72] T. Weinkauf and H. Theisel. Streak lines as tangent curves of a derived vector field. *IEEE TVCG (Proc. Visualization)*, 16(6):1225–1234, 2010.